



# Seismic evidence for partial melt below tectonic plates

Eric Debayle, Thomas Bodin, Stéphanie Durand, Yanick Ricard

## ► To cite this version:

Eric Debayle, Thomas Bodin, Stéphanie Durand, Yanick Ricard. Seismic evidence for partial melt below tectonic plates. *Nature*, 2020, 586 (7830), pp.555-559. 10.1038/s41586-020-2809-4 . hal-03006522

**HAL Id: hal-03006522**

**<https://hal.science/hal-03006522>**

Submitted on 19 Nov 2020

**HAL** is a multi-disciplinary open access archive for the deposit and dissemination of scientific research documents, whether they are published or not. The documents may come from teaching and research institutions in France or abroad, or from public or private research centers.

L'archive ouverte pluridisciplinaire **HAL**, est destinée au dépôt et à la diffusion de documents scientifiques de niveau recherche, publiés ou non, émanant des établissements d'enseignement et de recherche français ou étrangers, des laboratoires publics ou privés.

# Seismic evidence for partial melt below tectonic plates

Eric Debayle<sup>1</sup>, Thomas Bodin<sup>1</sup>, Stéphanie Durand<sup>1</sup> and Yanick Ricard<sup>2</sup>

<sup>1</sup>Univ Lyon, Univ Lyon 1, ENSL, CNRS, LGL-TPE, F-69622, Villeurbanne, France

<sup>2</sup>Univ Lyon, ENSL, Univ Lyon 1, CNRS, LGL-TPE, F-69007, Lyon, France

The seismic low velocity zone (LVZ) of the upper mantle is generally associated with a low-viscosity asthenosphere that plays a key role for the dynamics of plate tectonics<sup>1</sup>. However, its origin remains enigmatic, some authors attributing the reduction in seismic velocity to a small amount of partial melt<sup>2,3</sup>, others invoking solid-state mechanisms near the solidus<sup>4–6</sup>, or the effect of volatile contents<sup>6</sup>. Observations of shear attenuation provide additional constraints to unravel the origin of the LVZ<sup>7</sup>. Here, we report the discovery of partial melt within the LVZ from the simultaneous interpretation of global 3D shear attenuation and velocity models. We observe that partial melting down to 150-200 km depth beneath mid-ocean ridges, major hotspots and back-arc regions feeds the asthenosphere. A small part of this melt (<0.30%) remains trapped within the oceanic LVZ. The amount of melt is related to plate velocities and increases significantly between 3 and 5 cm yr<sup>-1</sup>, similar to previous observations of mantle crystal alignment underneath tectonic plates<sup>8</sup>. Our observations suggest that by reducing viscosity<sup>9</sup>, melt facilitates plate motion and large-scale crystal alignment in the asthenosphere. Melt is absent under most of the continents.

Our finding results from the simultaneous analysis of two upper mantle tomographic models of shear wave velocity ( $V_s$ ) and attenuation (parameterised

with  $Q_s$  the quality factor, a measure of energy dissipation). Until now, most global tomographic studies of the upper mantle and their thermochemical interpretation have focused on shear velocity<sup>4,7</sup>. Recent experiments on olivine suggest that wave speed and attenuation are insensitive to water, which would imply that elevated water contents are not responsible for the LVZ<sup>10</sup>. However,  $V_s$  is sensitive to temperature, composition and melt content, and deciphering the causes of its variations represents a strongly non-unique inverse problem, severely limiting our understanding of the Earth's interior. Shear attenuation has a different sensitivity to these quantities, and therefore provides complementary constraints on the origin of seismic heterogeneities<sup>11</sup>. Shear attenuation is negligibly dependent on major element chemistry<sup>12</sup>, and exponentially dependent on temperature<sup>13</sup>. The relation between attenuation and melt is debated, with some authors arguing for a weak dependence based on experiments, models and seismological observations<sup>12</sup>, while others suggest a larger effect<sup>3</sup>. Measuring shear attenuation is nevertheless difficult. For this reason, only a few global  $Q_s$  models have been published in the last 20 years<sup>14</sup>, and the only recent joint interpretation of 3D  $Q_s$  and  $V_s$  tomographic models at global scale is based on models built from different datasets and modeling approaches<sup>15</sup>.

The novelty of our study is to simultaneously interpret two recent global  $V_s$  and  $Q_s$  models that are consistent as obtained from the same Rayleigh wave dataset, at the same resolution and using the same modelling approach. These  $V_s$  (DR2020s) and  $Q_s$  (QsASR17) models are displayed in **Figure 1**. Details of our tomographic procedure can be found in Methods. Before interpreting these two models in the light of laboratory experiments, a few words are needed to emphasize in what temperature and pressure range our interpretation is pertinent. The attenuation models derived by mineral physicists<sup>4,13</sup> are valid for temperatures  $T$  larger than 900°C, which correspond to the base of the lithosphere and to the asthenosphere.

They consider thermally activated processes varying exponentially with  $1/T$  that would imply quality factor in excess of 2,000 in the upper 100 km of the lithosphere and reaching several million near the surface (see Methods). However, finite  $Q_s$  is observed in the crust and in the cold mantle lithosphere where attenuation is most likely related to non-thermal processes such as scattering or fluid-fracture interactions<sup>14</sup>. Furthermore, the attenuation observed in seismology accumulates along the seismic ray and the observation of  $Q_s$  is only possible when the amplitude of a wave is measurably smaller than in a pure elastic model. Given the uncertainties on amplitude data, it appears impossible to resolve quality factors larger than  $\sim 2,000$  with long period Rayleigh waves (at periods of 100s, assuming velocities of  $4.5 \text{ km s}^{-1}$  and ray lengths of 10,000 km, the amplitude reduction with respect to a pure elastic model, would be less than 3.5%). Our inversion leads indeed to a  $Q_s$  model with strong lateral variations, by two orders of magnitudes, but with a maximum  $Q_s$  of  $\sim 1,750$ . Our attenuation model is therefore mostly adapted to depths greater or equal to  $\sim 100 \text{ km}$ , where  $Q_s$  values between fifty and a few hundreds are expected<sup>15</sup>. Therefore, our interpretation applies to the oceanic asthenosphere and the mantle structure at depths greater or equal to  $\sim 100 \text{ km}$ , where our tomographic models are accurate and where conditions similar to those used in laboratory experiments prevail.

**Figure 2** displays  $Q_s$  as a function of  $V_s$  for each pixel of the maps, at different depths in the upper mantle. The curves in dark and light blue represent the theoretical relations due to temperature variations for a meltless pyrolitic mantle<sup>16</sup>, given by two anelasticity models<sup>4,13</sup> based on laboratory experiments, appropriate for asthenospheric conditions (see Methods for details). These models only explain a limited part of the velocities and attenuations of our dataset. We consider that the first theoretical curve<sup>4</sup> is compatible with a given  $V_s$ - $Q_s$  observation if it falls within the typical uncertainties of the  $V_s$  and  $\ln(Q_s)$



observations, 1% and 10% respectively (ivory colour). We show in Methods and supplementary **Figures S1-10** that reconciling the low values of  $V_s$  with  $Q_s$  cannot be done by invoking radial anisotropy, elastically accommodated grain boundary sliding, or the effect of composition or water. However, this can be done by adding partial melt, thus reducing  $V_s$ , and shifting the theoretical curves to the left in **Figure 2**, since as discussed below, adding partial melt reduces  $V_s$  but has little effect on  $Q_s$ . Warm colours in **Figure 2** indicate the amount of melt ( $<0.7\%$ ) needed to reconcile observations with the first theoretical model<sup>4</sup> (dark blue curve), which requires the smallest amount of melt. On the right side of the ivory region, points in grey are those for which  $V_s$  is too high compared to the theoretical value. They are associated with the lithospheric depletion of cratonic roots. In this case, the grey intensity quantifies the departure in percent from the theoretical curve assuming a meltless pyrolitic mantle. Results using the second theoretical model<sup>13</sup> are shown in **Figures S11-12**. They lead essentially to the same conclusions, but require larger melt fractions (up to 1%), which are more difficult to reconcile with the very small melt fraction ( $\sim 0.1\%$ ) suggested by geochemical studies<sup>4</sup>.

The effect of melt on  $V_s$  has been estimated to 7.9% reduction per percent of melt based on model calculations<sup>17</sup>. Recent experiments<sup>3</sup> are in qualitative agreement but require a slightly larger  $V_s$  reduction (**Figure S13**). The effect of melt on attenuation is not well constrained and depends on the mechanisms of attenuation. We show in Methods that melt may have a large effect on  $Q_s$  at short period (1 s), but not in the period range of surface waves (50-250s). We therefore neglect the effect of melt on  $Q_s$  and we model its effect on  $V_s$  based on recent experiments<sup>3</sup>. **Figure 2** shows that the slowest shear velocities require less than 0.7 % of melt.

**Figure 3** displays global maps of melt content at different depths, using the same colour-coding as in **Figure 2**. The associated mantle temperatures, derived by our approach are on average slightly above the solidus in oceanic regions, between 100 and 200 km depth (**Figure S14, panel g**). The differences between the maps of temperature (**Figure S14 panels a-f**) and those of melt content are attributed to a variable amount of volatile<sup>9</sup>. A higher amount of volatiles above subduction zones may lower the solidus and favor melting, while a dryer mantle in other regions may impede melting. The heterogeneities in **Figure 3** display a strong correlation with surface tectonics. Regions where  $V_s$  is too high (in grey) are located beneath continents down to 150 km depth. The discrepancy is likely due to our assumption of a homogeneous and pyrolitic mantle. This assumption is reasonable in the well-mixed convective mantle. However, beneath cratons, compositional heterogeneities and depletion of incompatible elements are contributing to the high seismic velocities. Our observations under cratons, at 150 km depth, are on average 2.4% faster than a pyrolitic mantle which is compatible with compositional effects<sup>18</sup>.

At 100 km depth, melt is required below mid-ocean ridges, some hotspots near the Atlantic ridge and in the south Pacific Ocean, back-arc basins around the Pacific Ocean including the eastern margin of Asia and some other active tectonic regions (Afar, Tibet, West of North-America and Southwest Pacific, including the North Fidji basin and the Northfolk ridge south of the Vanuatu arc). In these regions, the amount of melt exceeds 0.3% and can reach 0.7%. Melt is not required beneath most of the remaining oceanic and continental Phanerozoic lithosphere where temperature variations alone explain our observations.

The depth range 150-200 km corresponds to the oceanic LVZ, where a small amount of melt (<0.3%) is required over broad regions. The largest amount is

beneath hotspots, ridges, and volatile-rich back-arc regions and can extend deeper than the LVZ, suggesting that these deep regions feed the asthenosphere with partial melt. For example, partial melt is observed down to 250 km beneath Hawaii and 300 km beneath the Afar and East-African rift, the hotspots located on the western part of North-America, the region of the Balleny Islands in Antarctica, the western Pacific and the Indian ocean near the Ninety-East ridge. A melting anomaly near 300 km on the eastern part of the Tibetan plateau is also observed.

The depth extent and amount of melt beneath oceanic regions are consistent with local studies. The NoMELT experiment<sup>19</sup> was performed beneath a location relatively far away from Pacific hotspots (blue star in **Figure 3**) where we too confirm the absence of melt in what could be a volatile-poor mantle. We observe melting beneath the East Pacific Rise (green star in **Figure 3**) down to 250 km depth, in agreement with the MELT experiment<sup>20</sup>. The depth extent of melting beneath Hawaii down to 250 km is supported by measurements of water abundance in the deep region that feeds the plume<sup>21</sup>. Our results agree with observations of significant melting beneath the Philippine Sea plate and the Western Pacific<sup>2</sup>. Finally, melting down to at least 300 km beneath the Balleny Islands hotspot is also consistent with previous observations<sup>22</sup>.

The origin of partial melt within most of the oceanic LVZ is uncertain. Melting at mid ocean-ridges can exceed 1% in the depth range 40-80 km<sup>20,23</sup>, but smaller volume melting may occur down to depths of 150-250 km<sup>23</sup>. After melting at mid-ocean ridges, a small amount of melt may remain unextractable from the mantle peridotite<sup>9,24,25</sup>. Our observations suggest that decompression melting with at least 0.3 to 0.7% of melt occurs also beneath some hotspots and back arc basins down to about 200 km. Most of the melt produced in these regions is extracted and incorporated to the oceanic crust, but a small amount remains in the oceanic LVZ

as it ages. The quantity of melt, if any, decreases close to continents below 0.1%, where a simple model without melt explains most of our observations. This may be due to the difficulty of melting the depleted continental lithosphere. However under tectonically active regions, beneath the Afar and East-African rifts, Tibet, Western North-America and Transantarctic Mountains, the asthenosphere contains a small amount of melt (**Figure 3**).

The quantity of melt needed to reconcile Vs and Qs under large swaths of the oceanic LVZ is larger than usual estimates of unextractable melt, which range from very small values<sup>9</sup> to a maximum of 0.1%<sup>24</sup>. Although melt is likely connected and able to percolate even at very small porosity<sup>9</sup>, surface tension resists the phase separation<sup>9,26</sup>. The ability of the melt to rise depends on various parameters, surface tension, buoyancy, permeability, melt and matrix viscosities, which are all known with large uncertainties<sup>25</sup>. The melt fractions greater than 0.1% that we obtain are therefore plausible. This melt concentration is in overall agreement with the range of estimates derived from electromagnetic studies<sup>27</sup> of the LVZ, which often propose even larger values (see Methods). A structure made of magma-rich sills embedded in a meltless mantle might also be mapped by tomography as an average medium with moderate melt content. This partially molten layered model has been proposed for the northwest Pacific and Philippine plates<sup>2</sup>, but it could extend more generally to the entire oceanic LVZ. This layering would explain both the radial anisotropy observed within the oceanic LVZ<sup>28</sup> and the sharp velocity and viscosity contrasts at the lithosphere-asthenosphere boundary<sup>2</sup>.

Finally, the amount of melt exhibits a very peculiar relation with the plate velocity<sup>29</sup> expressed in a no-net-rotation reference frame (**Figure 4**). The melt fraction in the asthenosphere, abruptly increases by a factor close to 2 when the

velocity is larger than 4 cm yr<sup>-1</sup>. This variation is very similar to the observed variation of azimuthal anisotropy with present-day plate motion<sup>8</sup>. Our results suggest that plate-scale crystal alignment beneath fast-moving plates is associated with a greater amount of melt. This requires either that melt facilitates deformation<sup>9</sup> or that deformation favours melt retention in the LVZ<sup>2</sup>, or both. In any case, the small amount of melt observed beneath large swaths of the oceanic LVZ is likely to significantly decrease viscosity (by one to two orders of magnitude<sup>9</sup>, see Methods) and to play a significant role in the decoupling of tectonic plates from the mantle.

#### References from main text:

1. Ricard, Y., Doglioni, C. & Sabadini, R. Differential rotation between lithosphere and mantle - a consequence of lateral mantle viscosity variations. *J. Geophys. Res.* **96**, 8407–8415 (1991).
2. Kawakatsu, H. *et al.* Seismic Evidence for Sharp Lithosphere-Asthenosphere Boundaries of Oceanic Plates. *Science* **324**, 499–502 (2009).
3. Chantel, J. *et al.* Experimental evidence supports mantle partial melting in the asthenosphere. *Sci. Adv.* **2**, (2016).
4. Takei, Y. Effects of Partial Melting on Seismic Velocity and Attenuation: A New Insight from Experiments. in *Annu. Rev. Earth Planet. Sci.* (ed. Jeanloz, R and Freeman, K.) **45**, 447–470 (2017).
5. Faul, U. H. & Jackson, I. The seismological signature of temperature and grain size variations in the upper mantle. *Earth Planet. Sci. Lett.* **234**, 119–134 (2005).
6. Karato, S. ichiro. On the origin of the asthenosphere. *Earth Planet. Sci. Lett.* **321–322**, 95–103 (2012).
7. Cobden, L., Trampert, J. & Fichtner, A. Insights on Upper Mantle Melting, Rheology, and Anelastic Behavior From Seismic Shear Wave Tomography. *Geochem., Geophys., Geosy.*, **19**, 3892–3916 (2018).
8. Debayle, E. & Ricard, Y. Seismic observations of large-scale deformation at the bottom of fast-moving plates. *Earth Planet. Sci. Lett.* **376**, (2013).
9. Holtzman, B. K. Questions on the existence, persistence, and mechanical effects of a very small melt fraction in the asthenosphere. *Geochemistry, Geophys. Geosystems* **17**, 470–484 (2016).
10. Cline, C. J., Faul, U. H., David, E. C., Berry, A. J. & Jackson, I. Redox-influenced seismic properties of uppermantle olivine. *Nature* **555**, 355–358 (2018).
11. Deschamps, F., Konishi, K., Fuji, N. & Cobden, L. Radial thermo-chemical structure beneath Western and Northern Pacific from seismic waveform inversion. *Earth Planet. Sci. Lett.* **520**, 153–163 (2019).
12. Shito, A., Karato, S., Matsukage, K. & Nishihara, Y. Towards Mapping the Three-Dimensional Distribution of Water in the Upper Mantle From Velocity and Attenuation Tomography. *Washingt. DC Am. Geophys. Union Geophys. Monogr. Ser.* **168**, (2006).
13. Jackson, I., Fitz Gerald, J. D., Faul, U. H. & Tan, B. H. Grain-size-sensitive seismic wave attenuation in polycrystalline olivine. *J. Geophys. Res., Sol. Earth.*, **107**, 2360 (2002).
14. Romanowicz, B. A. & Mitchell, B. J. 1.25 - Deep Earth Structure: Q of the Earth from Crust to Core. in *Treatise on Geophysics (Second Edition)* (ed. Schubert, G.) 789–827 (Elsevier, 2015).

- doi:<https://doi.org/10.1016/B978-0-444-53802-4.00021-X>
15. Dalton, C. A., Ekström, G. & Dziewonski, A. M. Global seismological shear velocity and attenuation: A comparison with experimental observations. *Earth Planet. Sci. Lett.* **284**, 65–75 (2009).
  16. Xu, W., Lithgow-Bertelloni, C., Stixrude, L. & Ritsema, J. The effect of bulk composition and temperature on mantle seismic structure. *Earth Planet. Sci. Lett.* **275**, 70–79 (2008).
  17. Hammond, W. C. & Humphreys, E. D. Upper mantle seismic wave velocity: Effects of realistic partial melt geometries. *J. Geophys. Res. Solid Earth* **105**, 10975–10986 (2000).
  18. Bruneton, M. *et al.* Layered lithospheric mantle in the central Baltic Shield from surface waves and xenolith analysis. *Earth Planet. Sci. Lett.* **226**, 41–52 (2004).
  19. Lin, P. Y. P. *et al.* High-resolution seismic constraints on flow dynamics in the oceanic asthenosphere. *Nature* **535**, 538–541 (2016).
  20. Yang, Y., Forsyth, D. W. & Weeraratne, D. S. Seismic attenuation near the East Pacific Rise and the origin of the low-velocity zone. *Earth Planet. Sci. Lett.* **258**, 260–268 (2007).
  21. Wallace, P. J. Water and partial melting in mantle plumes: Inferences from the dissolved H<sub>2</sub>O concentrations of Hawaiian basaltic magmas. *Geophys. Res. Lett.* **25**, 3639–3642 (1998).
  22. Sieminski, A., Debayle, E. & Lévêque, J.-J. Seismic evidence for deep low-velocity anomalies in the transition zone beneath West Antarctica. *Earth Planet. Sci. Lett.* **216**, (2003).
  23. Key, K., Constable, S., Liu, L. & Pommier, A. Electrical image of passive mantle upwelling beneath the northern East Pacific Rise. *Nature* **495**, 500+ (2013).
  24. Faul, U. H. Melt retention and segregation beneath mid-ocean ridges. *Nature* **410**, 920–923 (2001).
  25. Selway, K. & O'Donnell, J. P. A small, unextractable melt fraction as the cause for the low velocity zone. *Earth Planet. Sci. Lett.* **517**, 117–124 (2019).
  26. Hier-Majumder, S., Ricard, Y. & Bercovici, D. Role of grain boundaries in magma migration and storage. *Earth Planet. Sci. Lett.* **248**, 735–749 (2006).
  27. Ni, H., Keppler, H. & Behrens, H. Electrical conductivity of hydrous basaltic melts: Implications for partial melting in the upper mantle. *Contrib. to Mineral. Petrol.* **162**, 637–650 (2011).
  28. Chang, S.-J. J., Ferreira, A. M. G. G., Ritsema, J., van Heijst, H. J. & Woodhouse, J. H. Joint inversion for global isotropic and radially anisotropic mantle structure including crustal thickness perturbations. *J. Geophys. Res. Solid Earth* **120**, 4278–4300 (2015).
  29. DeMets, C., Gordon, R. G., Argus, D. F. & Stein, S. Effect of recent revisions to the geomagnetic reversal time-scale on estimates of current plate motions. *Geophys. Res. Lett.* **21**, 2191–2194 (1994).

**Acknowledgements.** We thank the Iris and Geoscope data centers for providing seismological data. We also thank two anonymous reviewers for their comments, J.P. Perrillat and M. Behn for discussions on mineralogy and attenuation models, and F. Dubuffet for preparing data for sharing as IRIS Data Products. The European Union Horizon 2020 research and innovation program funds T. B. under grant agreement 716542. The LABEX Lyon Institute of Origins (LIO, ANR-10-LABX-0066) of the University of Lyon funded a beowulf cluster hosted and maintained at ENSL, and used in this study. The world map figures were created with open software GMT 4.5.13.

**Author contributions.** E.D. and T.B. collaborated in developing the concept of this paper. E.D. wrote the codes for the interpretation of the seismic models and wrote the drafts of the manuscript. E.D. wrote the tomography code for Vs, Y.R. adapted this code for Qs. T.B. contributed to the design of the figures and to the writing of the manuscript. Y.R. developed preliminary codes for interpreting the seismic models, contributed to all mineralogical aspects and to the writing of the manuscript. S.D realized the tests of the effect of composition and contributed to the writing of the revised manuscript.

**Fig. 1: Shear velocity and attenuation in the upper mantle.** Panels a-c-e-g: perturbations in shear wave velocities from DR2020s shown in percent with respect to a mean value  $V_{\text{ref}}$  given in  $\text{km s}^{-1}$  above the colour scale. Panels b-d-f-h: maps of our Qs tomographic model QsADR17 at different depths in the upper mantle. Qs is plotted with a logarithmic scale. Its geometric average is given above the colour scale. Hotspot locations are shown with black triangles.

**Fig. 2: Scatter plot depicting the observed shear attenuation as a function of shear velocity compared with theoretical predictions.** The velocities (from DR2020s) and attenuation values (from QsADR17) are plotted at 100 km (panel a), 150 km (panel b) and 200 km depth (panel c). Each dot corresponds to a geographical location. The dark blue and light blue curves are the theoretical predictions assuming a pyrolitic composition<sup>34</sup> in the absence of melt using the anelasticity models of Takei<sup>4</sup> and Jackson et al.<sup>13</sup>, respectively. The upper colour scale indicates the amount of melt in percent required to explain our observations using Takei<sup>4</sup>'s model. Adding melt enables to lower the predicted velocity without changing Qs. The lower grey scale indicates the misfit in percent between theory and observations, in regions where Vs is too high and cannot be reconciled with model predictions assuming a pyrolitic mantle.

**Fig. 3: Melt content at different depths in the upper mantle.** This melt content is derived from the joint interpretation of QsADR17 and DR2020s. The colour coding is identical to Figure 2. Melt content in percent is indicated with warm colour from ivory (0% melt) to brown (0.4 to 0.7% melt). The grey scale indicates the misfit in percent between theory and observations, in regions where Vs is too high compared with predictions. Hotspots locations are indicated with black triangles. The blue and green stars indicate the location of the NoMELT and MELT experiments, respectively.

**Fig. 4: Percentage of melt at different depths as a function of absolute plate velocity.**

(The velocities<sup>29</sup> are expressed in a no-net-rotation reference frame. The percentage of melt is averaged for all geographical points with similar plate velocities, using a sliding window of  $\pm 2$  cm yr<sup>-1</sup>. The amount of melt increases significantly in the asthenosphere (100-200 km) for plate velocities between 3 and 5 cm yr<sup>-1</sup>. This result links with previous observations that only plates moving faster than 4 cm yr<sup>-1</sup> can organize the flow at large scale in the underlying asthenosphere<sup>8</sup>, suggesting that melt reduces viscosity<sup>9</sup> and facilitates large-scale crystal alignment.



## Methods

**Qs and Vs tomographic models.** Figure 1 presents maps of DR2020s, a new global Vs model and QsADR17 a recent global Qs model<sup>30</sup>. Both models are built from the same massive Rayleigh wave measurements<sup>31</sup>, and are obtained from a similar tomographic procedure. The first step is an automated waveform inversion approach which was applied to approximately 375,000 Rayleigh seismograms<sup>31</sup>. From a single surface wave seismogram, the waveform inversion extracts simultaneously a path-average depth-dependent shear velocity profile, Vs, and quality factor, Qs. By jointly interpreting the amplitude and phase of each waveform, we ensure that the interplay between Vs and Qs is accounted for, and that the shear quality factor and velocity profiles are constrained within the same period range. The waveform analysis is performed in the period range 50-250 s and accounts for the fundamental and up to the 5th higher mode of Rayleigh waves, thus ensuring a good depth resolution for Vs and Qs from 50 km depth down to the transition zone. It is a non-linear iterative process, which also produces frequency-dependent phase velocity and attenuation curves compatible with the recorded waveform. The effect of physical dispersion due to attenuation is accounted for in the modelling.

The second step is a regionalization of the 1D path-average models. DR2020s is obtained from the regionalization at each depth of the path-average Vs models using a continuous regionalization approach<sup>31</sup>. This tomographic inversion yields 3D absolute velocities. QADR17, a global model of Rayleigh-wave attenuation was obtained after adapting the same regionalization approach to our dataset of Rayleigh wave attenuation curves, parameterized as  $\ln(Q)$ <sup>32</sup>. The regionalisation of the path-average attenuation curves accounts for frequency-dependent effects like focussing-defocussing, which can have important effects on the amplitude of

Rayleigh waves. The logarithmic parameterization brings the distribution of the quality factor dataset close to a Gaussian, allows the large variations of  $Q$  documented by local seismic studies and guarantees to avoid negative attenuation values in the inverted model. The horizontal smoothing in DR2020s and QADR17 is determined by a Gaussian a priori covariance function controlled by an angular correlation length. Adenis et al.<sup>32</sup> chose a conservative value of  $10^\circ$  (meaning that the  $Q$  model is resolved accurately up to spherical harmonic 12). Debayle and Ricard<sup>31</sup> used a shorter correlation length of  $3.6^\circ$  for their  $V_s$  model DR2012. We re-inverted their dataset using a correlation length of  $10^\circ$  in order to obtain a  $S_v$ -wave tomographic model at the same horizontal resolution and vertical smoothing than QsADR17. To minimize biases due to un-modelled radial anisotropy, we computed the isotropic Voigt average of our  $S_v$  model and the  $Sh$  model obtained by adding the radial anisotropy of PREM to our  $S_v$  model. The resulting isotropic model DR2020s is plotted in **Figure 1**. Using other 1D or 3D models of radial anisotropy does not affect our conclusions, as discussed below. QsADR17 was obtained from the inversion at depth of QADR17<sup>30</sup>, using the same vertical smoothing as for DR2020s. DR2020s and QsADR17 are therefore consistent since they are derived from the simultaneous inversion of the same waveforms and inverted using the same regionalization approach with the same Gaussian filtering.

**Prediction of  $Q_s$  and  $V_s$  using a temperature-dependent model<sup>4</sup>.** The dark blue curve in **Figure 2** is obtained by predicting  $V_s$  and  $Q_s$  at each depth for a range of temperatures, using a temperature-dependent anelasticity model<sup>4</sup> and assuming a pyrolitic composition<sup>16</sup>. This model parameterizes the relaxation spectrum with a small number of variables determined from experimental data. It accounts for a monotonic background spectrum plus a broad temperature-dependent absorption peak in the seismic frequency band, whose amplitude and width increase below the solidus. This produces a significant enhancement of polycrystal anelasticity

before melting. This pre-melting effect induces large Vs reductions under the solidus. We choose the solidus according to Hirschman<sup>33</sup>. We use the model parameters given in Tables 1 and 2 of Takei<sup>4</sup>, except for the unrelaxed shear modulus  $\mu_U$ . We estimate  $\mu_U$  for a pyrolitic mantle using the mineralogic phase diagram computed by the Perple X software<sup>34</sup>. In **Figures S15-S16** we show the results obtained with the shear modulus of Takei<sup>4</sup>, which reduces the amount of melt in oceanic regions but fails to explain our  $\ln(Q_s)$ -Vs observations beneath old oceanic basins at 100 km depth. It also significantly increases the misfit beneath continents.

**Prediction of Qs and Vs from the experimental results of Jackson et al.<sup>13</sup>.** The light blue curve in **Figure 2** is obtained by a two-step process. First, we use experimental results on melt-free polycrystalline olivine to predict a theoretical quality factor  $Q_t$ . Computations are performed in the temperature range 800-1800 K and the pressure range 1.49-12.99 GPa, corresponding to the depth range 50-390 km. We use the following relation<sup>13</sup> :

$$Q_t^{-1}(T_0, T, P, d) = A \left( T_0 d^{-1} \exp(-(E + PV)/RT) \right)^\alpha \quad \text{Eq. A.1}$$

In this formulation,  $Q_t^{-1}$  at period  $T_0$  depends on the temperature  $T$ , the pressure  $P$  and to a lesser extent the grain size  $d$ .  $R$  is the gas constant,  $E$  is the activation energy and  $V$  is the activation volume. **Table S1** summarizes the values of the different parameters of Eq. A.1. In the range of values compatible with experiments<sup>13</sup>, we choose  $T_0=100$  s, the average period of our long period Rayleigh waves and  $d=0.01$ m. The theoretical curves corresponding to Eq. A1 are shown in **Figure S9**, with the effect of changing grain size.

Second, we use Perple X<sup>34</sup> to estimate an isotropic Vs for a pyrolitic model<sup>16</sup>. We compute Vs for the same temperatures and pressures as  $Q_t$ . Perple\_X produces

unrelaxed S-wave velocities at infinite frequency, above the absorption band of seismic attenuation, while our long period (>50 s) seismic surface waves are likely to see relaxed velocities. We therefore correct for the effect of anelasticity on  $V_s$ <sup>35</sup> :

$$V_s^t = V_{s\infty} \left( 1 - \frac{Q_t^{-1}(T_0, T, P, d)}{2 \tan(\pi \alpha / 2)} \right) \quad \text{Eq. A.2}$$

where  $V_{s\infty}$  is the unrelaxed velocity and  $V_s^t$  is the velocity corrected from the effect of attenuation. According to Eq. A2, the stronger the attenuation, the stronger the velocity reduction is. The light blue curve in **Figure 2** is finally obtained by plotting at a given depth the obtained  $\ln(Q_t)$  as a function of  $V_s^t$  for each temperature.

**Comparison between our observations and the theoretical relations.** At each geographical location and depth, we extract the observed value of  $Q_s$  in QsADR17 and  $V_s$  in DR2020s and we compare our observations with the chosen theoretical relation. We consider that a theoretical curve is compatible with a given  $V_s$ - $Q_s$  observation if it falls within  $\pm 1\%$  and  $\pm 10\%$  of the  $V_s$  and  $\ln(Q_s)$  observations, respectively (**Figure 2**). These errors are on the conservative side of recent estimates<sup>36,37</sup>. If the theoretical relation cannot explain our observations, two situations can arise: 1) the observed  $V_s$  is lower than the theoretical  $V_s^t$ . In this case melt can be added to reduce  $V_s^t$ . This is done assuming melt has no effect on  $Q_s$ ; 2) the observed  $V_s$  is higher than  $V_s^t$ . This is mostly the case under continents and can be explained by the depletion of the pyrolitic mantle increasing the theoretical  $V_s^t$ <sup>18</sup>.

**Effect of grain size.** Grain sizes in the shallow upper mantle are likely 1-20 mm as observed in upper mantle xenoliths, harzburgite and dunite bodies<sup>13</sup>. The effect of grain size on Eq. A1 is shown in **Figure S9**. The blue areas around the theoretical curves cover the influence of grain size from 1 mm (bottom dot curve) to an upper bound of 100 mm (upper dashed curve). For a given value of  $Q_s$ , increasing the

grain size increases the temperature and therefore decreases the velocity. As melt is required for explaining slow velocities, increasing grain size will decrease the amount of melt required to explain our observations. Using the equation A1 proposed by Jackson, we show in **Figure S12** melt distributions obtained for  $d=0.01$  m and in **Figure S17** those for the extreme value  $d=0.1$  m, which minimizes the amount of melt required in the LVZ. Maps in **Figure S17** are similar to those of **Figure S12** with a smaller amount of melt. However, in both cases, amounts of melt are larger than for our preferred model using the equations of Takei<sup>4</sup> (**Figure 3**).

**Amounts of melt.** Although the amount of melt present in the LVZ depends on the choice of the anelasticity model and on the effect of melt on  $V_s$ , we show in **Figures S12, S16, S17, S18** that different choices of parameters yields similar maps and that melt fractions away from source regions always stay below 1%, in agreement with the partially molten asthenosphere model<sup>2</sup>. We note however that our preferred anelasticity model<sup>4</sup> generally explains our  $V_s$  and  $\ln(Q_s)$  observations without the need of partial melt above and below the asthenosphere (**Figure 3**). This is therefore a conservative choice, able to reconcile our  $V_s$  and  $\ln(Q_s)$  observations in most of the upper mantle, while minimizing the amount of melt required in the LVZ.

**Effect of radial anisotropy.** We used the anisotropic parameter  $\xi=(V_{sh}/V_{sv})^2$  of PREM to convert our  $S_v$  observations into an isotropic model, DR2020s. We checked that 3D models of  $\xi$  obtained from anisotropic models like SEMUM2<sup>38</sup> or S362ANI<sup>39</sup> would not affect our main conclusions. As an example, **Figure S1** is similar to **Figure 3** but based on our  $S_v$  observations corrected with the anisotropic  $\xi$  parameters of SEMUM2 (**Figure S2**). Only minor changes are observed (for example in the Pacific or Indian oceans at 150 and 200 km), but

none that would change the interpretations of this paper. The lateral variations of  $\xi$  in SEMUM2 (**Figure S2**) are too small to affect our results. To confirm this point, we computed the anisotropy  $\xi$  that would be needed to account for the discrepancy between observed Qs and Vs, without invoking mantle depletion or partial melt (**Figure S3**). Comparison of this figure with **Figure S2** shows that neither the patterns nor the amplitude would fit (a 3 to 4 times larger anisotropy than in SEMUM2 would be needed to explain our observations). The anisotropy therefore does not affect our conclusions.

#### **Elastically accommodated grain boundary sliding (EAGBS) hypothesis.**

Anelastic relaxation caused by EAGBS can produce a sharp velocity reduction and may explain the LAB and the mid-lithosphere discontinuity observed beneath continents<sup>40</sup>. We tested the EAGBS hypothesis as an alternative explanation to partial melting for reconciling Vs and Qs in the LVZ. EAGBS is characterized by a sharp attenuation peak at a characteristic frequency  $\omega_{EAGBS}$ , followed by a diffused absorption band at lower frequencies. We first compute the characteristic frequency for the transition between unrelaxed and relaxed shear moduli. It is given by Karato et al.,<sup>40</sup> :

$$\omega_{EAGBS} = A \cdot d^{-1} \cdot \exp\left(-\frac{E^* + PV^*}{R \cdot T}\right) \cdot \left[1 + \left(\frac{C_w}{C_{w0}}\right)^r\right] \quad \text{Eq. A3}$$

where  $C_w$  is the water content in wt%,  $A=2.3 \times 10^{-14} \text{ m s}^{-1}$ ,  $C_{w0}=10^{-4} \text{ wt}\%$ ,  $r=1$ ,  $E^*=350 \text{ kJ mol}^{-1}$ ,  $V^*=10^{-6} \text{ m}^3$ ,  $d=5 \times 10^{-3} \text{ m}$ . Following Cobden et al.<sup>7</sup> we assume a dry mantle with  $C_w=10^{-6} \text{ wt } \%$ .

Surface waves analysed at frequencies lower than  $\omega_{EAGBS}$  should see relaxed velocities within the absorption band (see Fig. SI-2 of Karato et al.<sup>40</sup>), providing depth and temperature are within the activation ranges of EAGBS. EAGBS is activated between 60 and 160 km depth in the temperature range 900-1,350 K. We

consider that EAGBS may affect the interpretations of our long period ( $>40$  s) Qs and Vs maps when  $\omega_{EAGBS} > 0.025$  Hz and, from figure 4 of Karato et al.<sup>40</sup>, in the following temperature ranges for the depths of our tomographic inversion:

- 70 km: 930-1,140 K
- 90 km: 980-1,180 K
- 100 km: 1,010-1,220 K
- 125 km: 1,060-1,270 K
- 150 km: 1,130-1,330 K

Regions where EAGBS can apply are displayed in green in **Figure S4**. These regions correspond mostly to continental areas. Assuming that EAGBS correction applies, Karato et al.<sup>40</sup> list three alternative formulations for the velocity reduction. The Ghahremani<sup>41</sup> equation, which produces the smallest velocity reduction is :

$$V_s^{eagbs} = V_s^t \cdot \sqrt{\frac{0.86-0.83\nu}{1-\nu} \cdot \frac{1+\nu}{1.14+0.83\nu}} \quad \text{Eq. A.4}$$

where  $\nu$  is the Poisson's ratio ( $\sim 0.3$  for upper mantle minerals). Regions where this can reconcile our Vs and Qs observations are displayed in red in **Figure S4**. The two other formulations give too large velocity reduction. **Figure S4** shows that EAGBS fails at reconciling our long period observations, excepted in a few localized regions (in red). This does not preclude EAGBS to play a significant role in explaining the sharp velocity reduction associated with the LAB, which cannot be resolved by long period surface waves. However, the strong velocity reduction observed within the LVZ requires another mechanism.

**Effect of composition.** Compositional heterogeneities exist in the upper mantle, likely in the domain limited by pyrolite, harzburgite and pyroxenite<sup>42</sup>. Here, we check the effect of changing the composition from pyrolite to these end-members using Perple X<sup>34</sup> to compute the velocities. Pyroxenites have variable bulk

compositions<sup>43</sup> and we consider both a silica-deficient composition (see, Stixrude and Lithgow-Bertelloni<sup>44</sup>, Table 1) and a silica-excess composition similar to that of a subducted basalt (see, Xu et al.,<sup>16</sup>, Table 1). A silica-excess pyroxenite would only be faster than pyrolite after eclogitization, below 150 km depth (**Figure S5**, orange curve). At 100 km depth, a mantle made entirely of silica-excess pyroxenite would be too slow to explain the observed velocities (**Figure S6**). At larger depth, after eclogitization, it would lead to large melt fractions (**Figure S6**). The silica-deficient pyroxenite and the harzburgite are characterized at asthenospheric conditions by much faster or comparable velocities than pyrolite (**Figure S5**) and hence cannot explain the low velocities that we attribute to the presence of melt. Harzburgite would give melt fractions and distribution similar to pyrolite (**Figure S7**), while the silica-deficient pyroxenite would lead to higher melt fractions (up to 1.7%) and a ubiquitous melt presence below 150 km depth (**Figure S8**). Pyroxenite, whether enriched or depleted in silica, should only be present in a small proportion (~5%)<sup>42</sup> that hardly affects the seismic velocities of the peridotitic mantle. At any rate, large-scale chemical heterogeneities (> 1000 km) are not likely to exist in the LVZ, where viscosity is small (below 10<sup>20</sup> Pa s) and the convective mantle should be well stirred and mixed. Therefore, our observations cannot be explained by reasonable variations of compositions in the LVZ.

**Possible effect of water.** Although, it has been recently shown that in olivine, wave-speed and attenuation are insensitive to water<sup>10</sup>, some previous studies had suggested an effect of water quantified following the equation<sup>45</sup>:

$$Q_t^{-1}(T_0, T, P, C_{OH}, d) = A \left( T_0 d^{-1} \left( \frac{C_{OH}}{C_{OH(ref)}} \right)^r \exp(-(E + PV)/RT) \right)^\alpha \quad \text{Eq. A.5}$$

where  $C_{OH}$  is the water concentration,  $r$  is a dimensionless constant and all other parameters are as in Eq. A1. The average H<sub>2</sub>O content of Earth's upper mantle is estimated in the range 50-200 ppm<sup>46</sup>. We test a value close to the upper bound



( $C_{OH}=1000H/10^6$  Si, corresponding to  $125 \pm 75$  ppm by weight of water) with  $r=1$ , a standard value for moderate water content and  $C_{OH(ref)}=50H/10^6$  SI<sup>7</sup>. The corresponding theoretical curves are shown in blue on **Figure S9**. At fixed temperature, water increases attenuation. However to keep Q constant, an increase of water content must be balanced by a decrease of temperature and therefore by a higher expected velocity  $V_s^t$ . Reconciling this higher  $V_s^t$  with our observations requires larger amounts of melt (**Figure S10**). Therefore, if there were an effect of water on Vs and Qs, it would increase the required amount of melt.

**Effect of melt on attenuation.** A small amount of melt might have a large effect on attenuation<sup>47</sup> in the case of grain boundary sliding, where a broad dissipation peak is observed in the seismic frequency band. Body wave studies have reported low Qs values at short period (1s) with  $Q_s \leq 25$  beneath the Juan de Fuca and Gorda ridges<sup>48</sup> and  $25 \leq Q_s \leq 80$  in the back-arc mantle of Central America, the Marianas and the Lau Basin<sup>49</sup>. A recent experimental study suggests that 0.2% of melt produces  $Q_s=48$ <sup>3</sup>. However such a large effect of melt on Qs is difficult to reconcile with long period (>30 s) surface waves observations of  $Q_s=80$  beneath the fast spreading southern East Pacific Rise<sup>20</sup> where up to 1-2% of melt is expected<sup>50</sup>. If the attenuation mechanism is melt squirt, then the dissipation peak may lie outside the seismic frequency band and cause little attenuation. Model calculations<sup>51</sup>, long-period surface waves<sup>20</sup> and experiments<sup>12</sup> favour such interpretation. This is also supported by our long period (100 s) global surface wave tomographic models, which suggest that strong Vs and Qs reductions are not necessarily correlated<sup>30,32</sup>. For these reasons, we assume that in the period range of surface waves (50-250s), melt does not significantly affect attenuation and we neglect its effect on Qs.

**Temperature in the upper mantle.** Our Qs and Vs seismic models are interpreted using mineral physics results<sup>4,13</sup>. These experimental results are valid at temperatures

larger than 900°C or 1000°C, which are reached at the base of the lithosphere and in the asthenosphere. The predictions of our model can be checked with respect to the well-known thermal behaviour of the cooling oceanic lithosphere<sup>52,53</sup> although this is certainly pushing the model outside its applicability range. **Figure S19 (panel a)**, displays the temperature variations beneath the Pacific as a function of sea-floor age predicted from our seismic models using experimental results<sup>4</sup>. It demonstrates that even at depths shallower than 100 km, we retrieve the well-known age-dependence of temperature in oceanic regions (we also pick up the cold signal of the West Pacific subductions at old ages). However, our temperature variations between the ridge and an old lithosphere (~100°) are lower than the predictions of the plate-cooling model (250° at 75 km depth, **panel b**). **Panel c** displays the quality factors that would be deduced from the plate-cooling model using the experimental results<sup>4</sup> used in this paper. In the oceanic lithosphere,  $Q_s$  values much greater than 2000 ( $\ln(Q_s) > 7.6$ ) would be predicted, that cannot be retrieved by long period seismology. The limitations of experimental data at low temperatures together with the inability of surface wave seismology to quantify precisely negligible attenuations, explain why we do not interpret results at depths shallower than 100 km. Below the oceanic plates, **Figure S14, panel g** shows that our predicted temperatures beneath oceans are perfectly compatible with geodynamic and petrologic expectations. In agreement with our findings, under oceans, the average 1D temperature profile is above the solidus<sup>4</sup> and the adiabat<sup>54</sup> in the depth range 100-200 km, where we predict partial melting. This overshoot of the temperature, above the adiabat, is indeed found in all numerical simulations of mantle convection<sup>55</sup>. Under continents, the temperature appears to be below the solidus<sup>4</sup> and the adiabat<sup>54</sup>. It reaches the adiabat around 250 km depth (**Figure S14, panel g**).

**Compatibility of our results with electrical conductivity.** Our results are consistent with the interpretation of a number of recent studies of electrical

conductivity. In the depth range 100-150 km, the joint interpretation of electrical and seismic data<sup>56</sup> requires 0.3-2.5% of melt beneath the mid-Atlantic ridge, 1% or less melt beneath Hawaiï and less than 5% of melt beneath the East-pacific rise, in good agreement with **Figure 3**. We also confirm the absence of melt in the region of the NoMELT experiment<sup>19</sup>, in agreement with conductivity data in this region<sup>25</sup>. Previous experimental results suggest that between 0.3 and 2% of hydrous basaltic melt can account for the observed electrical conductivity in the LVZ<sup>27</sup>. A more recent study<sup>57</sup> has refined these results by simultaneously measuring wave velocity and electrical conductivity on a simplified partial melt analogue. They conclude that the low velocity zone away from spreading ridges can be explained by 0.3-0.8% volatile-bearing melt, the upper bound of our observations.

**Implications for viscosity.** The variation of viscosity as a function of melt content occurs in two steps<sup>9</sup>. The onset of melting brings already a significant effect on viscosity when a connected network of melt tubules is formed. The viscosity  $\eta$  is expected to decrease by one or two orders of magnitude before the melt fraction  $\phi$  reaches 0.1%. For larger melt content,  $\eta$  decreases further<sup>9</sup> with  $d\ln(\eta)/d\phi = -26$  but this effect is minor for the low melt content that we observe. Under oceanic plates where  $\phi$  is around 0.3%,  $\eta$  should be one or two orders of magnitude lower than under continents.

**Data availability:** The dataset generated during this study (3D Vs, Qs models and melt fraction models) is available as IRIS data products at <https://doi.org/10.17611/dp/emc.2020.dbrdnature.1>.

**Code availability:** Numerical modelling codes related with this paper can be downloaded from <https://doi.org/10.17611/dp/emc.2020.dbrdnature.1>. Requests about the numerical modelling codes associated with this paper should be sent to

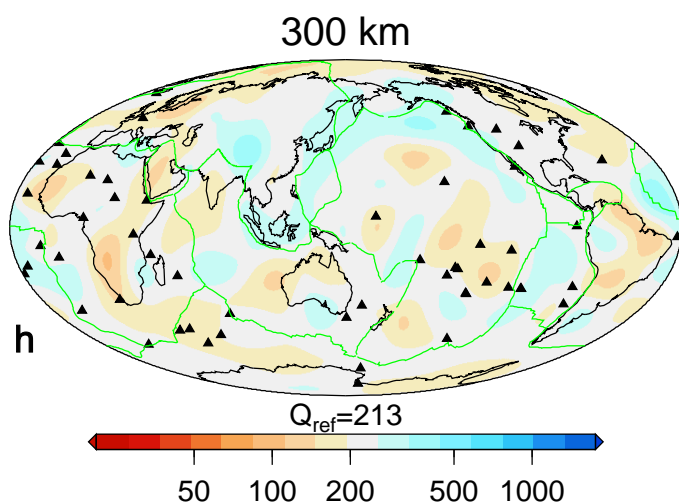
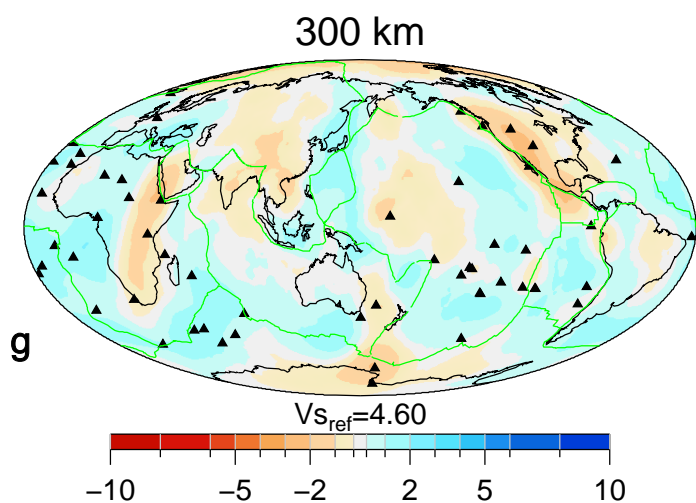
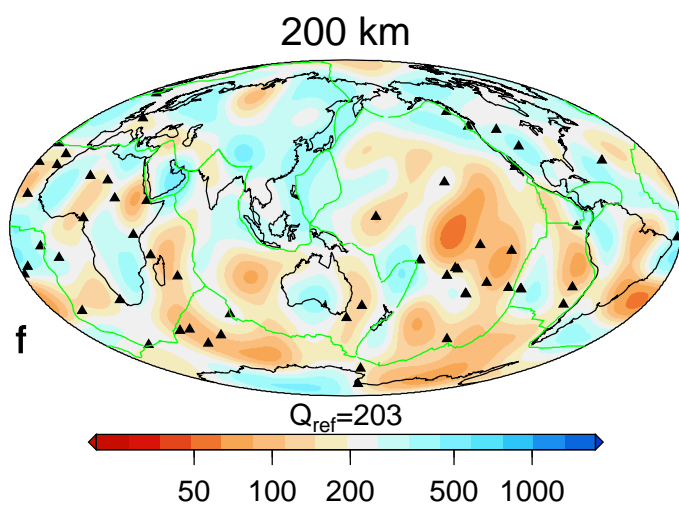
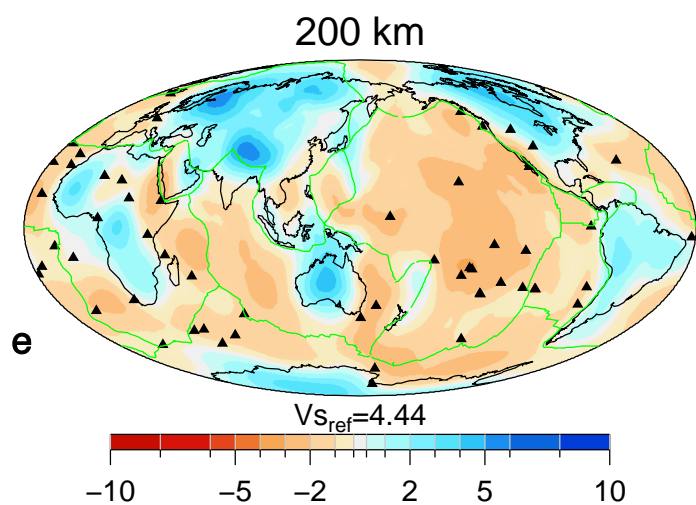
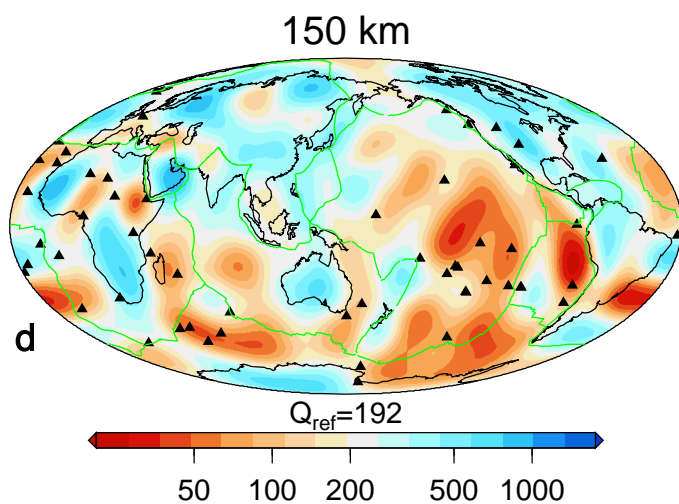
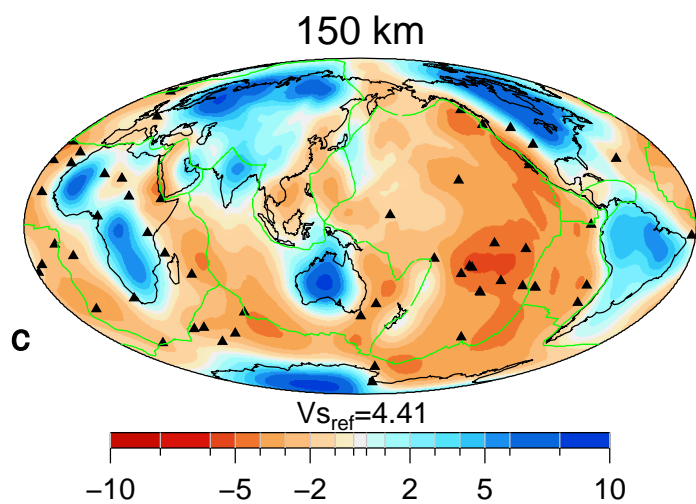
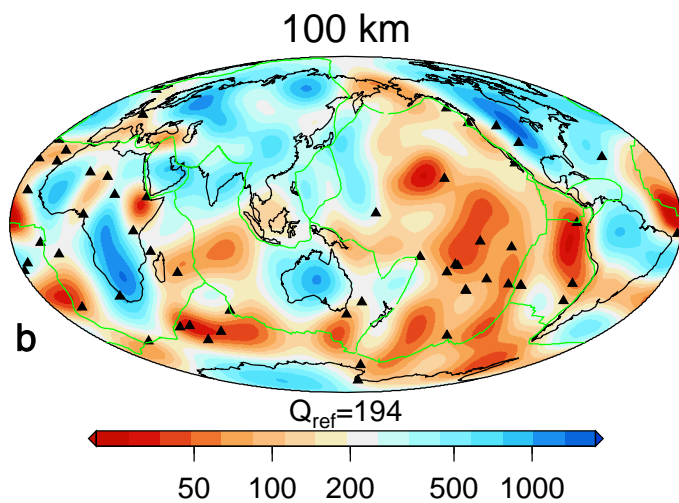
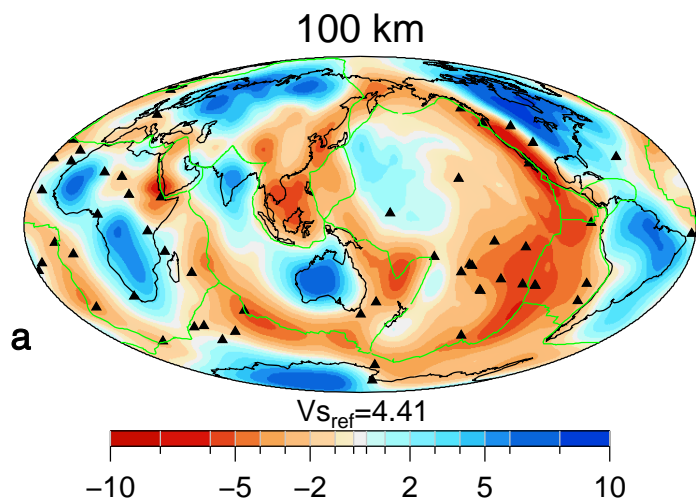
Eric.Debayle@ens-lyon.fr. Most figures were created with open software GMT  
4.5.13.

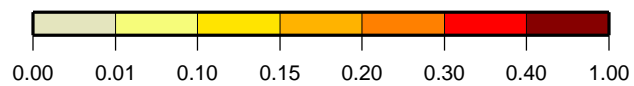
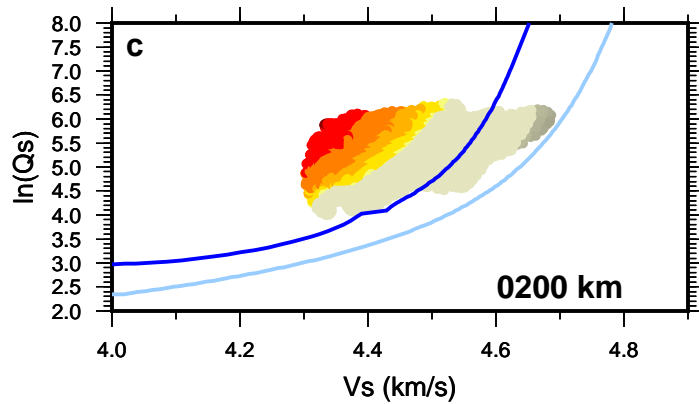
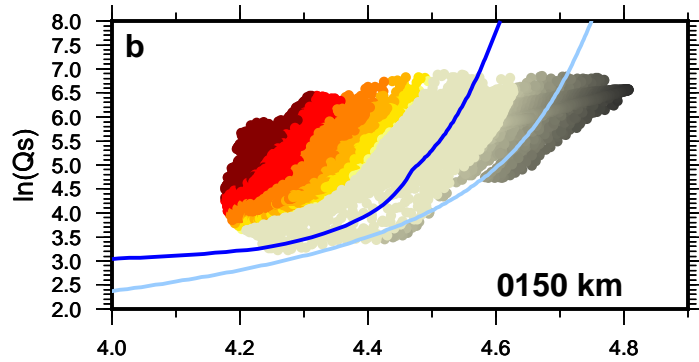
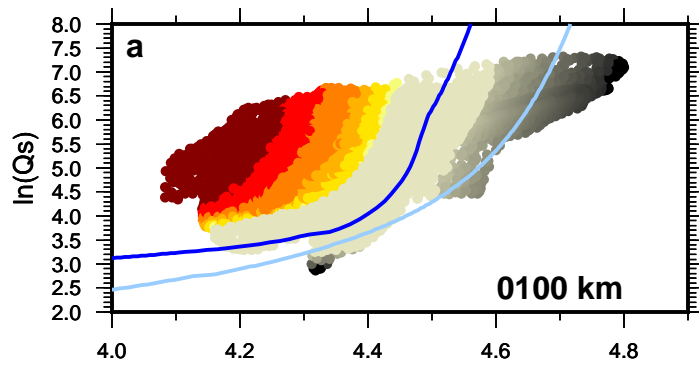
**Competing interest:** The authors declare no competing interests.

## References from Methods:

30. Adenis, A., Debayle, E. & Ricard, Y. Attenuation tomography of the upper mantle. *Geophys. Res. Lett.* **44**, (2017).
31. Debayle, E. & Ricard, Y. A global shear velocity model of the upper mantle from fundamental and higher Rayleigh mode measurements. *J. Geophys. Res., Sol. Earth.*, **117**, (2012).
32. Adenis, A., Debayle, E. & Ricard, Y. Seismic evidence for broad attenuation anomalies in the asthenosphere beneath the Pacific Ocean. *Geophys. J. Int.* **209**, 1677–1698 (2017).
33. Hirschmann M. M. Mantle solidus: Experimental constraints and the effects of peridotite composition. *Geochemistry Geophys. Geosystems* **1**, 1042 (2000).
34. Connolly, J. A. D. Computation of phase equilibria by linear programming: A tool for geodynamic modeling and its application to subduction zone decarbonation. *Earth Planet. Sci. Lett.* **236**, 524–541 (2005).
35. Karato, S. Importance of anelasticity in the interpretation of seismic tomography. *Geophys. Res. Lett.* **20**, 1623–1626 (1993).
36. Zaroli, C. Global seismic tomography using Backus-Gilbert inversion. *Geophys. J. Int.* **207**, 876–888 (2016).
37. Resovsky, J., Trampert, J. & der Hilst, R. D. Error bars for the global seismic Q profile. *Earth Planet. Sci. Lett.* **230**, 413–423 (2005).
38. French, S., Lekic, V. & Romanowicz, B. Waveform Tomography Reveals Channeled Flow at the Base of the Oceanic Asthenosphere. *Science* **342**, 227–230 (2013).
39. Kustowski, B., Ekstrom, G. & Dziewonski, A. M. Anisotropic shear-wave velocity structure of the Earth's mantle: A global model. *J. Geophys. Res.* **113**, (2008).
40. Karato, S. I., Olugboji, T. & Park, J. Mechanisms and geologic significance of the mid-lithosphere discontinuity in the continents. *Nat. Geosci.* **8**, 509–514 (2015).
41. Ghahremani, F. Effect of grain boundary sliding on anelasticity of polycrystals. *Int. J. Solids Struct.* **16**, 825–845 (1980).
42. Hirschmann, M. M. & Stolper, E. M. A possible role for garnet pyroxenite in the origin of the “garnet signature” in MORB. *Contrib. Miner. Pet.* **124**, 185–208 (1996).
43. Lambart, S., Laporte, D. & Schiano, P. Markers of the pyroxenite contribution in the major-element compositions of oceanic basalts: Review of the experimental constraints. *Lithos* **160**, 14–36 (2013).
44. Stixrude, L. & Lithgow-Bertelloni, C. Mineralogy and elasticity of the oceanic upper mantle: Origin of the low-velocity zone. *J. Geophys. Res. Solid Earth* **110**, B03204 (2005).
45. Behn, M. D., Hirth, G. & Elsenbeck, J. R. Implications of grain size evolution on the seismic structure of the oceanic upper mantle. *Earth Planet. Sci. Lett.* **282**, 178–189 (2009).
46. Hirschmann, M. M. Water, melting, and the deep Earth H<sub>2</sub>O cycle. *Annu. Rev. Earth Planet. Sci.* **34**, 629–653 (2006).
47. Faul, U. H., Fitz Gerald, J. D. & Jackson, I. Shear wave attenuation and dispersion in melt-bearing olivine polycrystals: 2. Microstructural interpretation and seismological implications. *J. Geophys. Res. Solid Earth* **109**, 1–20 (2004).
48. Eilon, Z. C. & Abers, G. A. High seismic attenuation at a mid-ocean ridge reveals the distribution of deep melt. *Sci. Adv.* **3**, (2017).
49. Abers, G. A. *et al.* Reconciling mantle attenuation-temperature relationships from seismology, petrology, and laboratory measurements. *Geochem., Geophys., Geosy.*, **15**, 3521–3542 (2014).

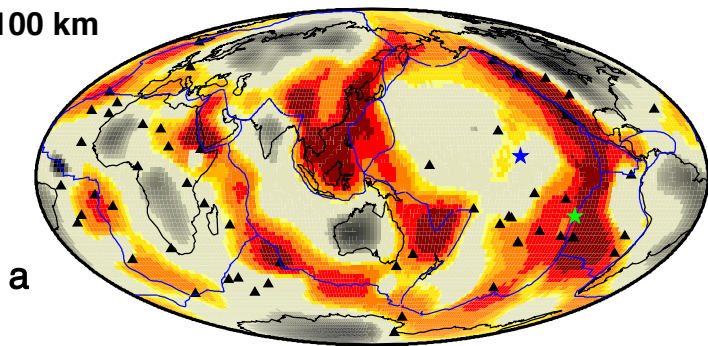
- 653 50. Dunn, R. A. & Forsyth, D. W. Imaging the transition between the region of mantle melt  
654 generation and the crustal magma chamber beneath the southern East Pacific Rise with  
655 short-period Love waves. *J. Geophys. Res. Solid Earth* **108**, 2352 (2003).
- 656 51. Hammond, W. C. & Humphreys, E. D. Upper mantle seismic wave attenuation: Effects of  
657 realistic partial melt distribution. *J. Geophys. Res. Solid Earth* **105**, 10987–10999 (2000).
- 658 52. Turcotte, D. L. & Schubert, G. *Geodynamics: Applications of Continuum Physics to Geological*  
659 *Problems*. (John Wiley & Sons, New York, 1982).
- 660 53. Stein, C. A. & Stein, S. A model for the global variation in oceanic depth and heat flow with  
661 lithospheric age. *Nature*, **359**, 123–129 (1992).
- 662 54. Katsura, T. *et al.* Adiabatic temperature profile in the mantle. *Phys. Earth Planet. Inter.* **183**,  
663 212–218 (2010).
- 664 55. Curbelo, J. *et al.* Numerical solutions of compressible convection with an infinite Prandtl  
665 number: comparison of the anelastic and anelastic liquid models with the exact equations. *J.*  
666 *Fluid Mech.* **873**, 646–687 (2019).
- 667 56. Pommier, A. & Garnero, E. J. Petrology-based modeling of mantle melt electrical conductivity  
668 and joint interpretation of electromagnetic and seismic results. *J. Geophys. Res., Sol. Earth.*,  
669 **119**, 4001–4016 (2014).
- 670 57. Freitas, D., Manthilake, G., Chantel, J., Bouhifd, M. A. & Andrault, D. Simultaneous  
671 measurements of electrical conductivity and seismicwave velocity of partially molten  
672 geological materials: effect of evolving melt texture. *Phys. Chem. Miner.* **46**, 535–551 (2019).  
673



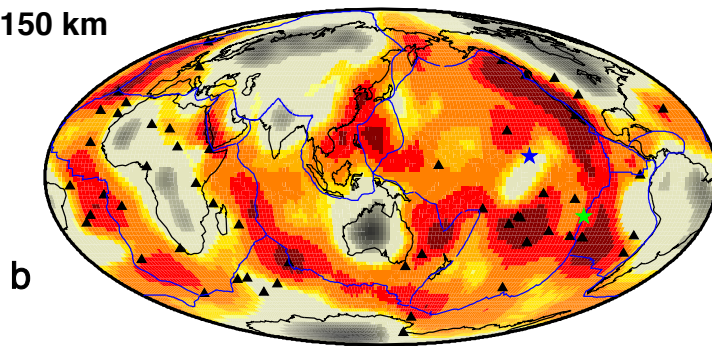




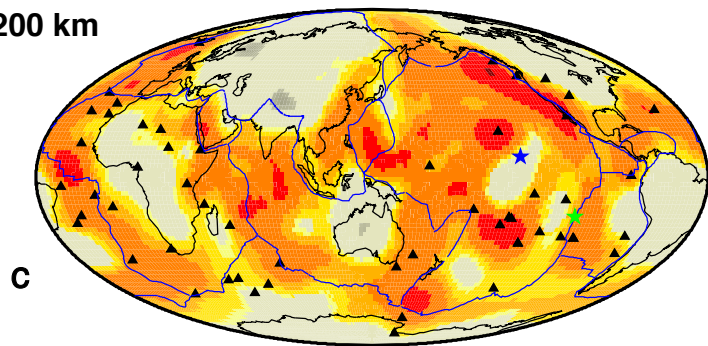
0100 km



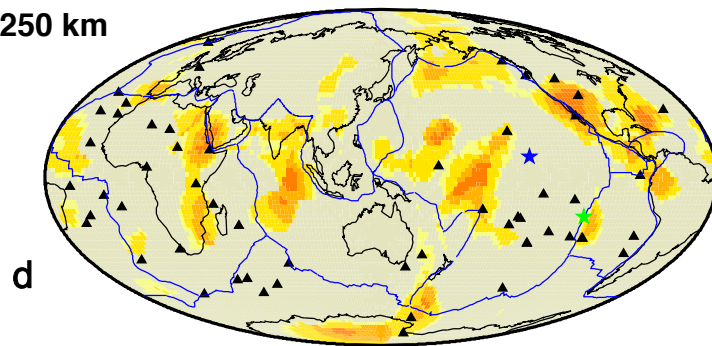
0150 km



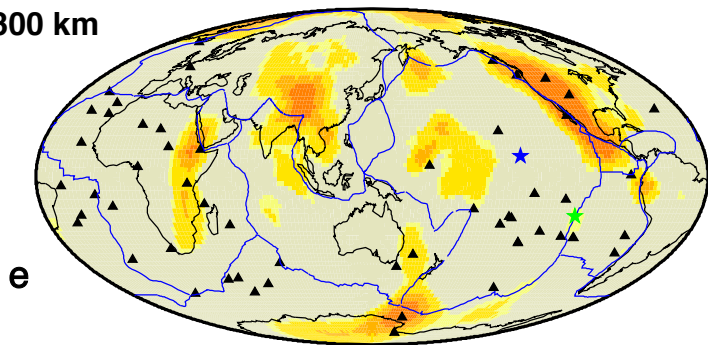
0200 km



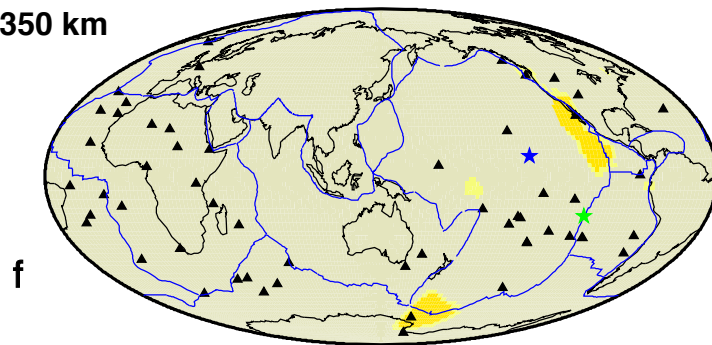
0250 km



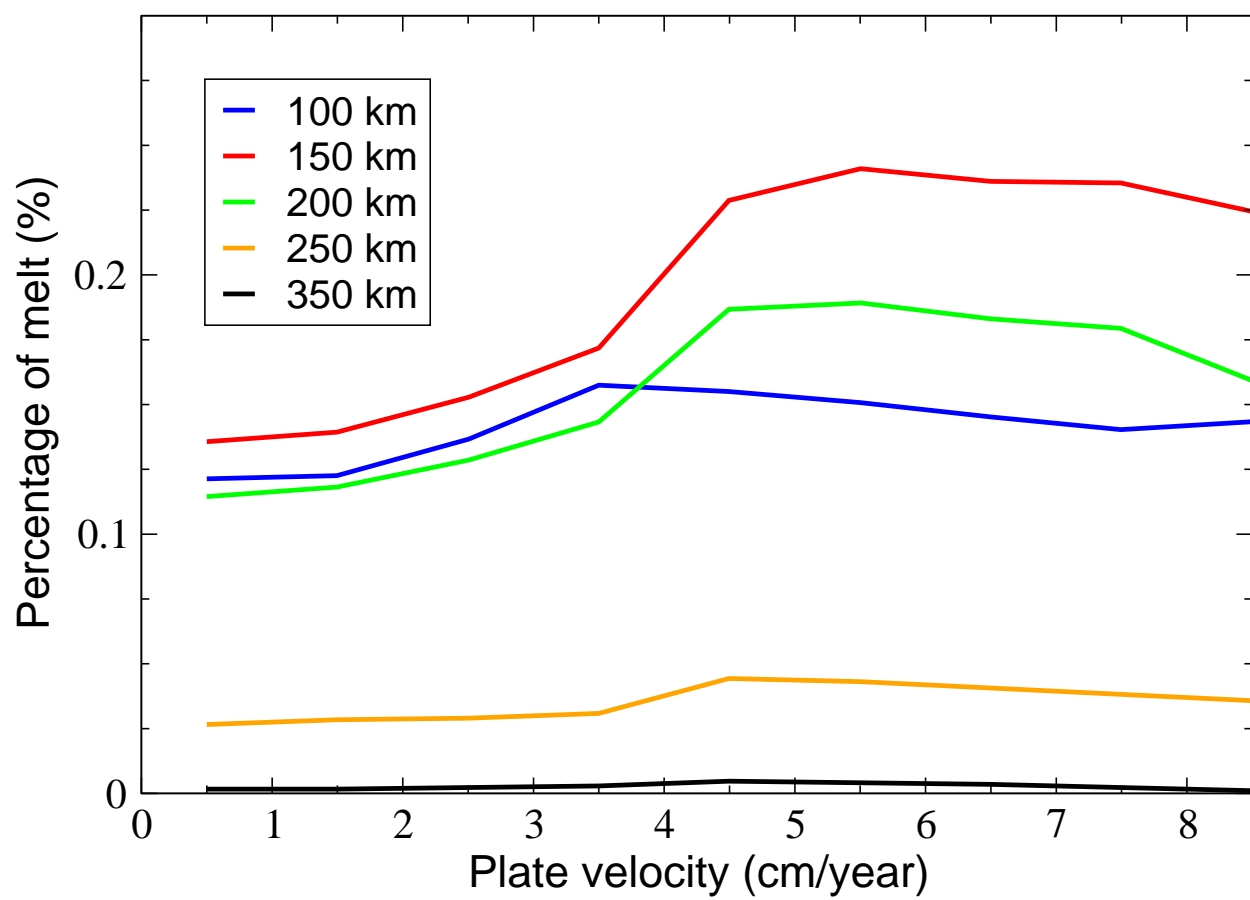
0300 km



0350 km







<i>Symbol</i>	<i>Description</i>	<i>Value</i>	<i>Units</i>
$\alpha$	exponent	0.26	
A	prefactor	$7.5 \times 10^{-2}$	$\text{s}^{-\alpha} \mu\text{m}^{\alpha}$
d	grain size	1-100	mm
$T_0$	period	100	s
E	activation energy	424	kJ/mol
V	activation volume	$6 \times 10^{-6}$	$\text{m}^3/\text{mol}$

Table S1: Reference parameters for Eq.A.1 after Jackson et al.<sup>1</sup>

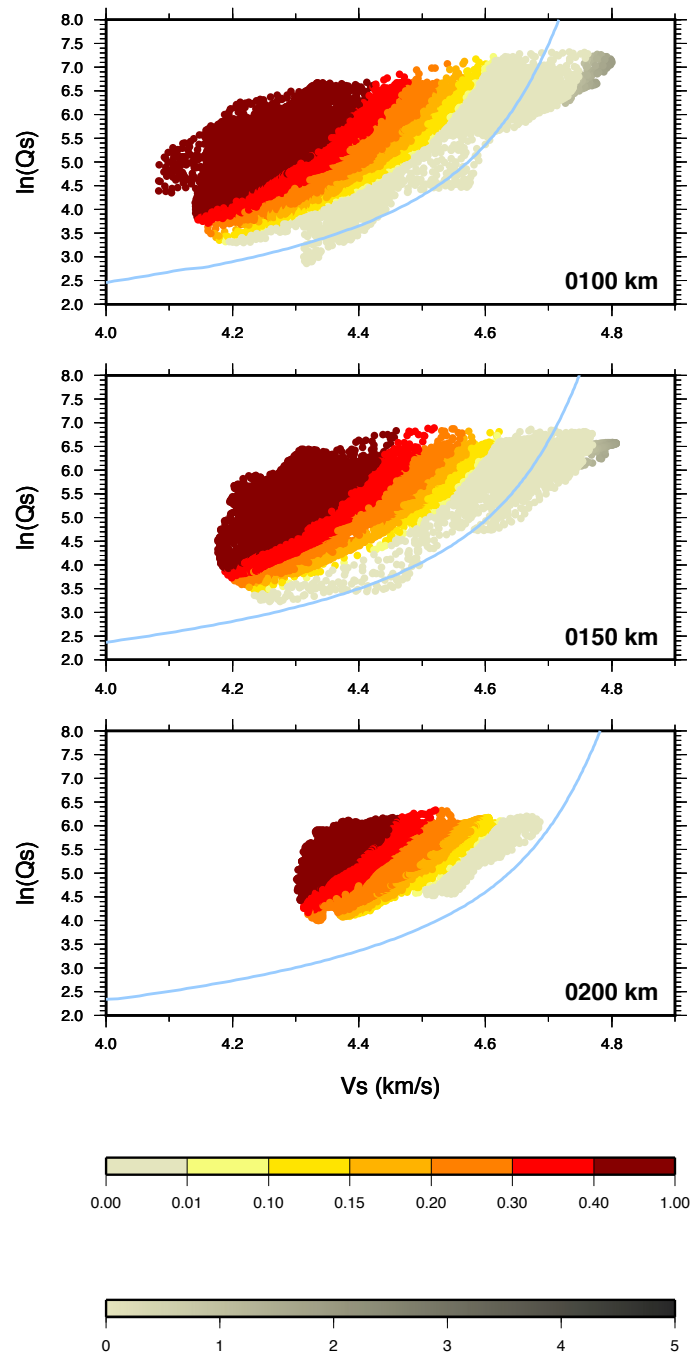


Fig. S1: same as Figure 2 but the color scales indicate the departure from the model of Jackson et al.<sup>1</sup> (light blue curve), for a grain size of 10 mm. The upper color scale indicates the amount of melt in percent required to explain our observations (ivory color from 0 to 0.01% of melt underlines data for which the model can reconcile our  $Q_s$  and  $V_s$  observations). The lower grey scale indicates the misfit in percent between theory and observations, in regions where  $V_s$  is too high and cannot be reconciled with model predictions.

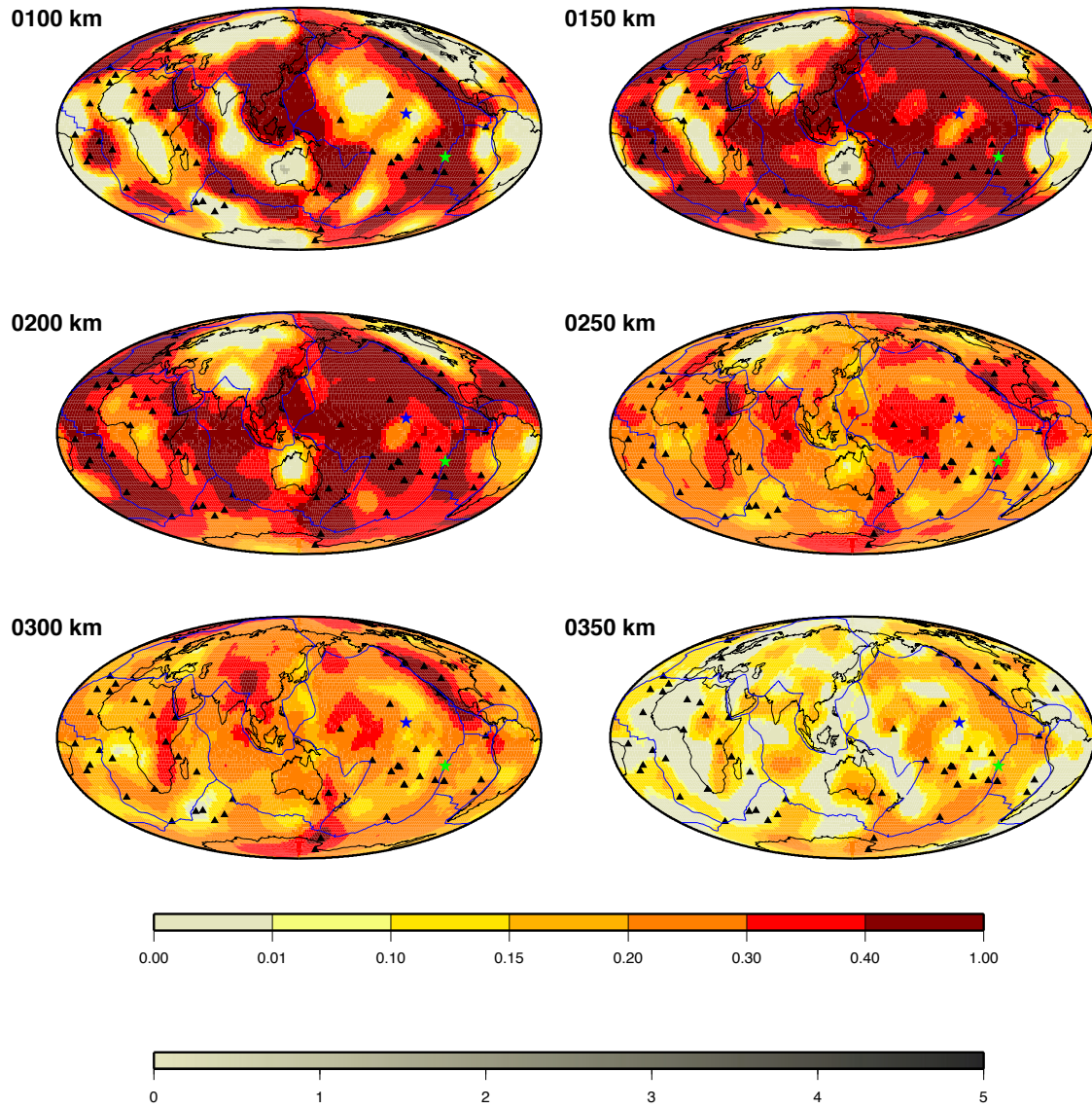


Fig. S2: same as Figure 3 but color scales indicate the departure from the model of Jackson et al.<sup>1</sup>, for a grain size of 10 mm. Melt content in percent is indicated with warm colors (upper color scale) from ivory (0% melt) to brown (0.4 to 0.7% melt). The lower grey scale indicates the misfit in percent between the theory and observations, in regions where  $V_s$  is too high compared with predictions.

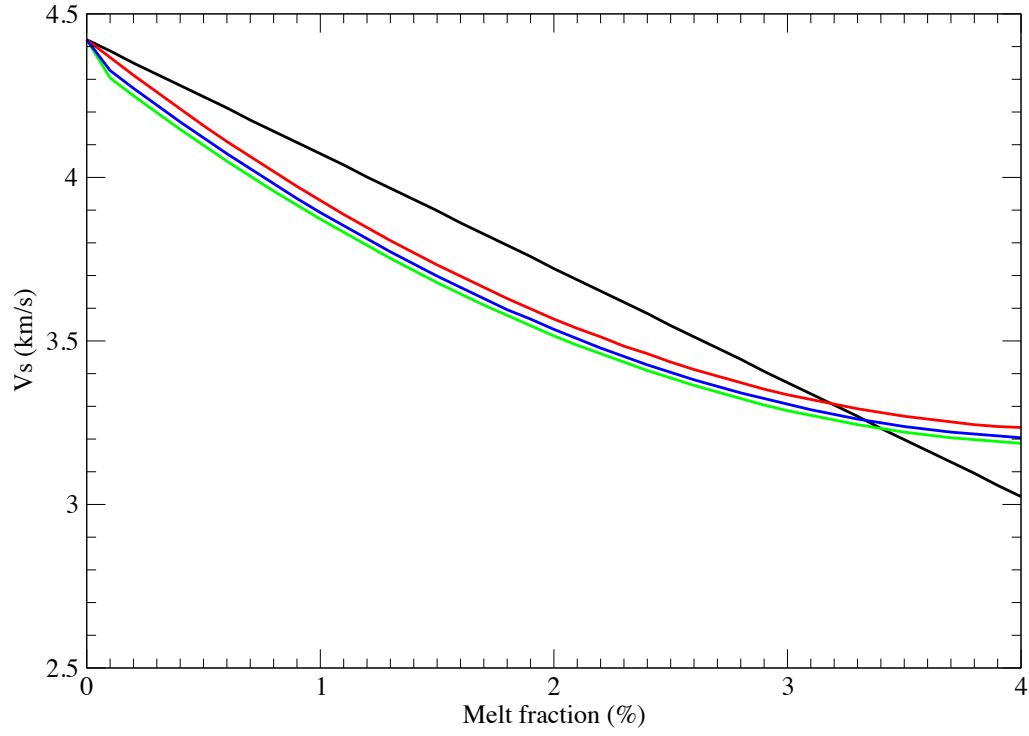


Fig. S3: Dependence of shear velocity on melt fraction  $\phi$ . The linear Vs reduction of 7.9% per percent of melt<sup>2</sup> is shown in black from a reference velocity  $V_{ref}$ . The polynomial expression ( $V_s = 0.065\phi^2 - 0.5565\phi + V_{ref}$ ) derived from experimental results<sup>3</sup> is shown in red. The anelastic effect expected for seismic waves at high temperature<sup>4</sup> is shown assuming  $Q_s=80$ , the value of PREM<sup>5</sup> in the asthenosphere, for two values of  $\alpha$  (blue curve for  $\alpha=0.38$  and green curve for  $\alpha=0.26$ ). For small melt fractions (<1%), a stronger Vs reduction is obtained using the polynomial expression and the choice of  $\alpha$  has a small effect.

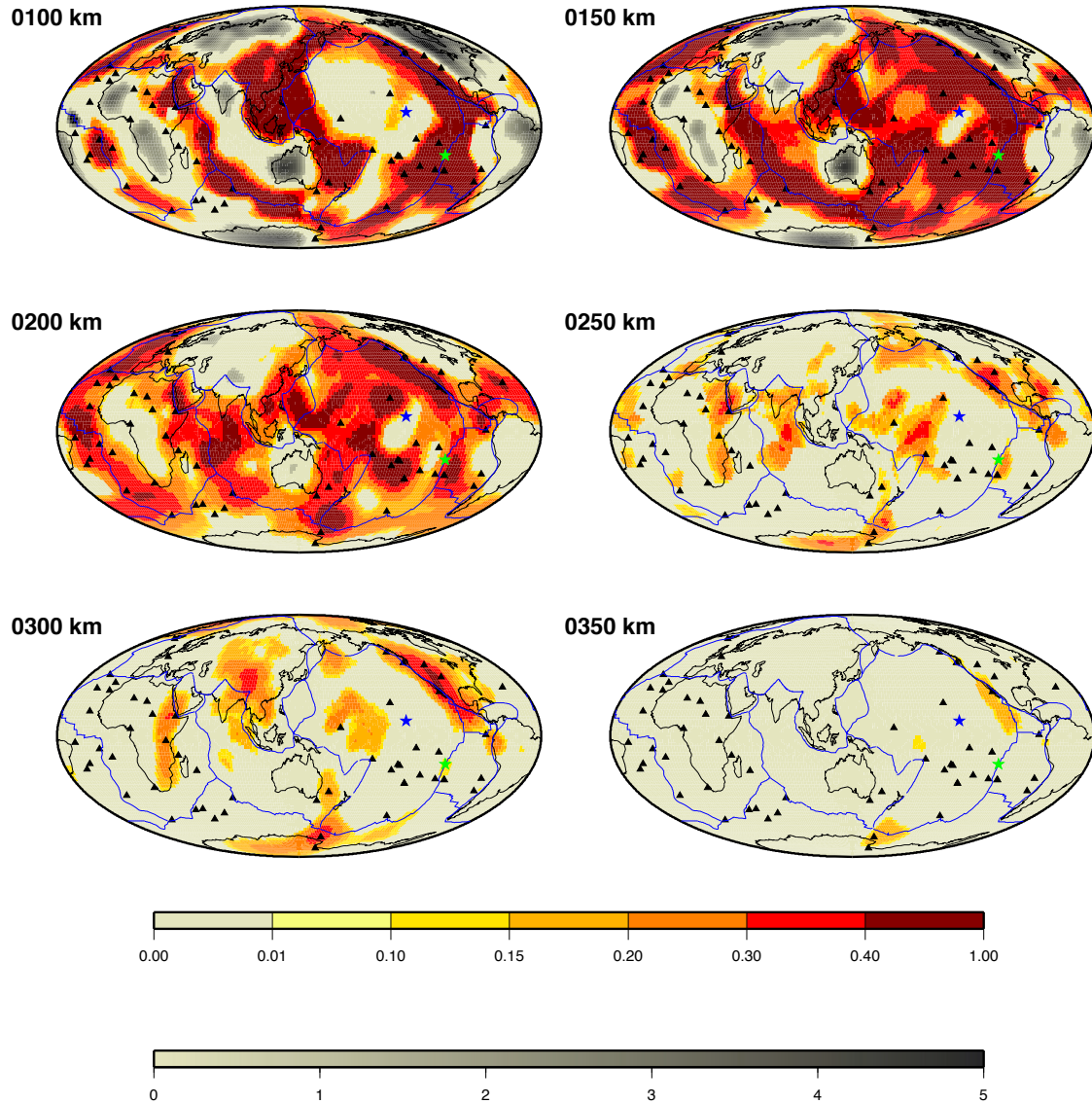


Fig. S4: same as Fig. 3 but using a linear 7.9% Vs reduction per percent of melt<sup>2</sup> instead of the polynomial expression derived from experimental results<sup>3</sup>. The upper color scale is slightly modified to allow melt content up to 1% (the maximum value at 100 km depth).

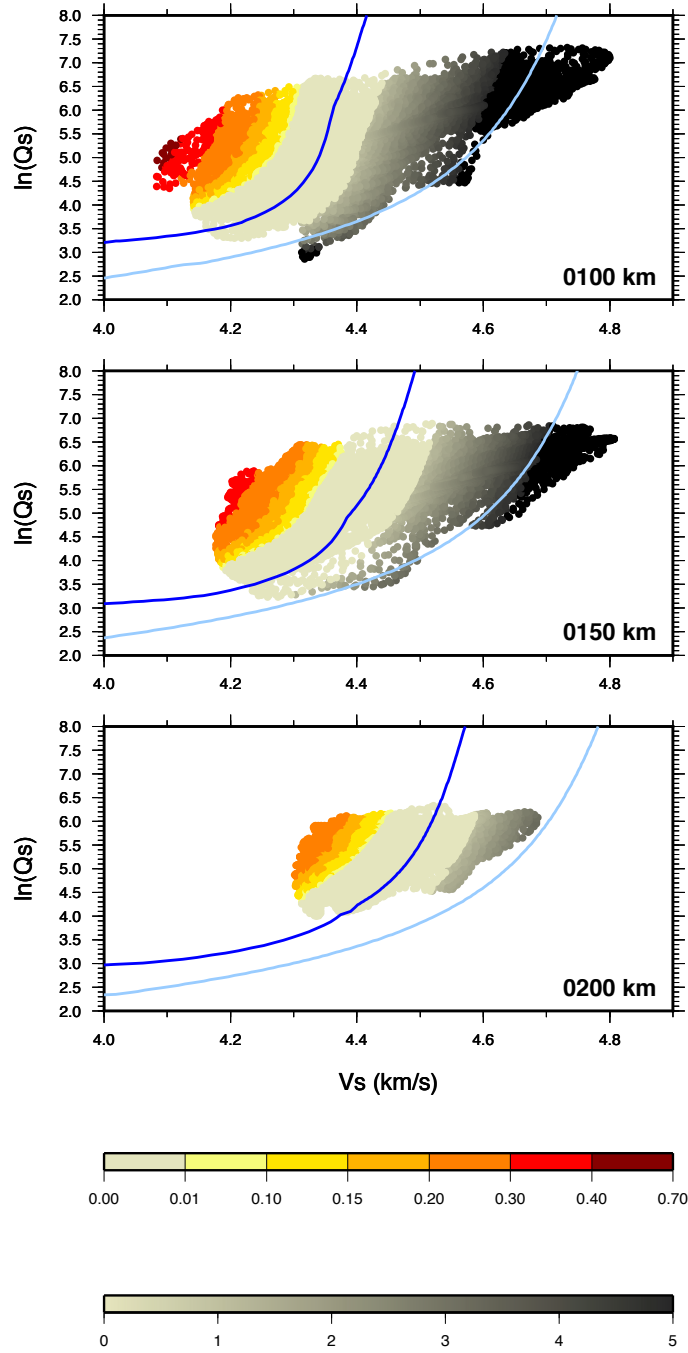


Fig. S5: same as Figure 2 but the unrelaxed shear modulus  $\mu_U$  needed to compute the temperature-dependent model (dark blue curve) is calculated using parameters proposed for of the temperature model of the Pacific<sup>6</sup>, instead of those deduced from Perple X assuming a pyrolitic composition.



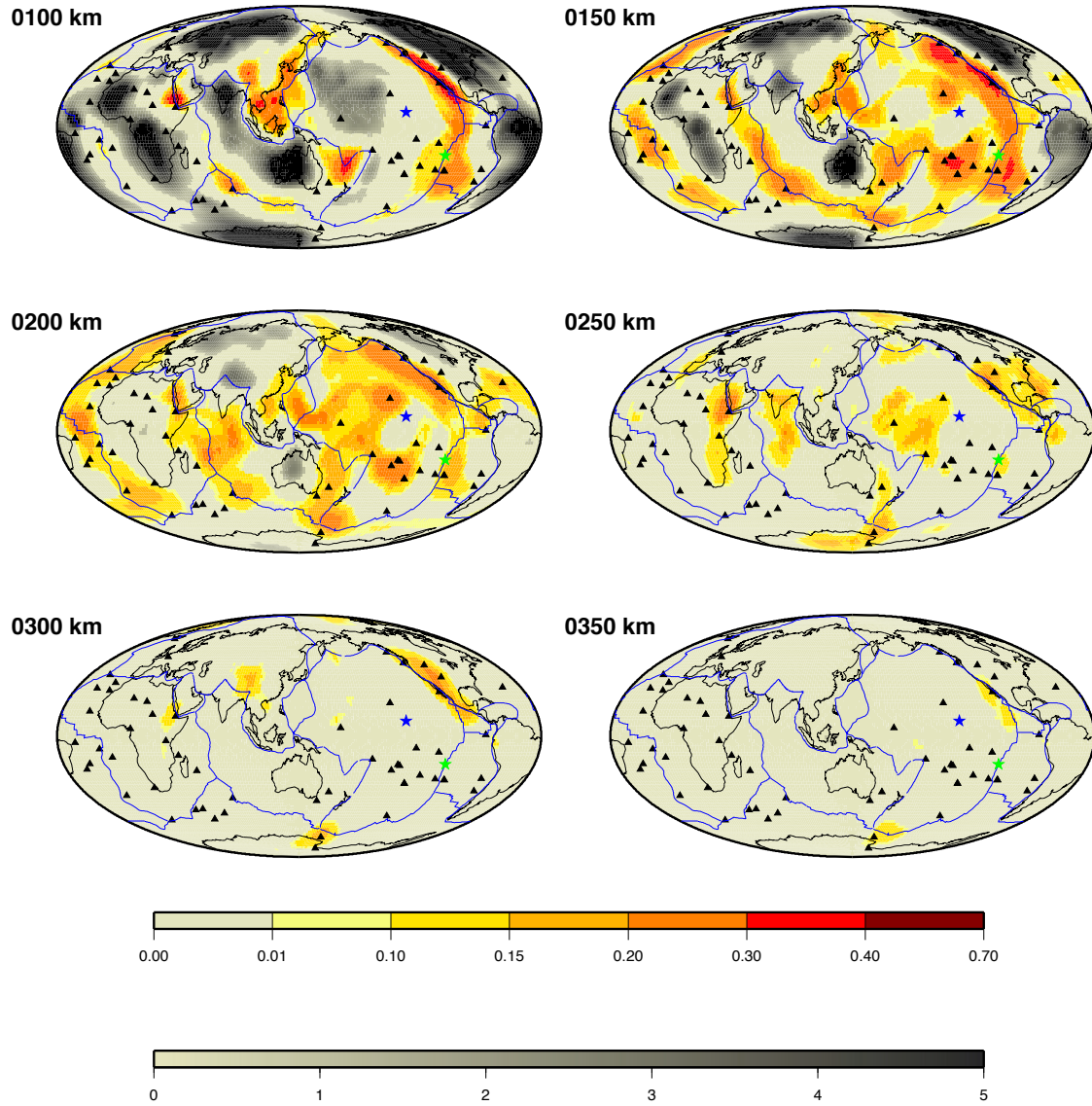


Fig. S6: same as Figure 3 but instead to estimate the unrelaxed shear modulus  $\mu_U$  using Perple X and a pyrolitic model, we use fitting parameters of the temperature model for the Pacific<sup>6</sup>.



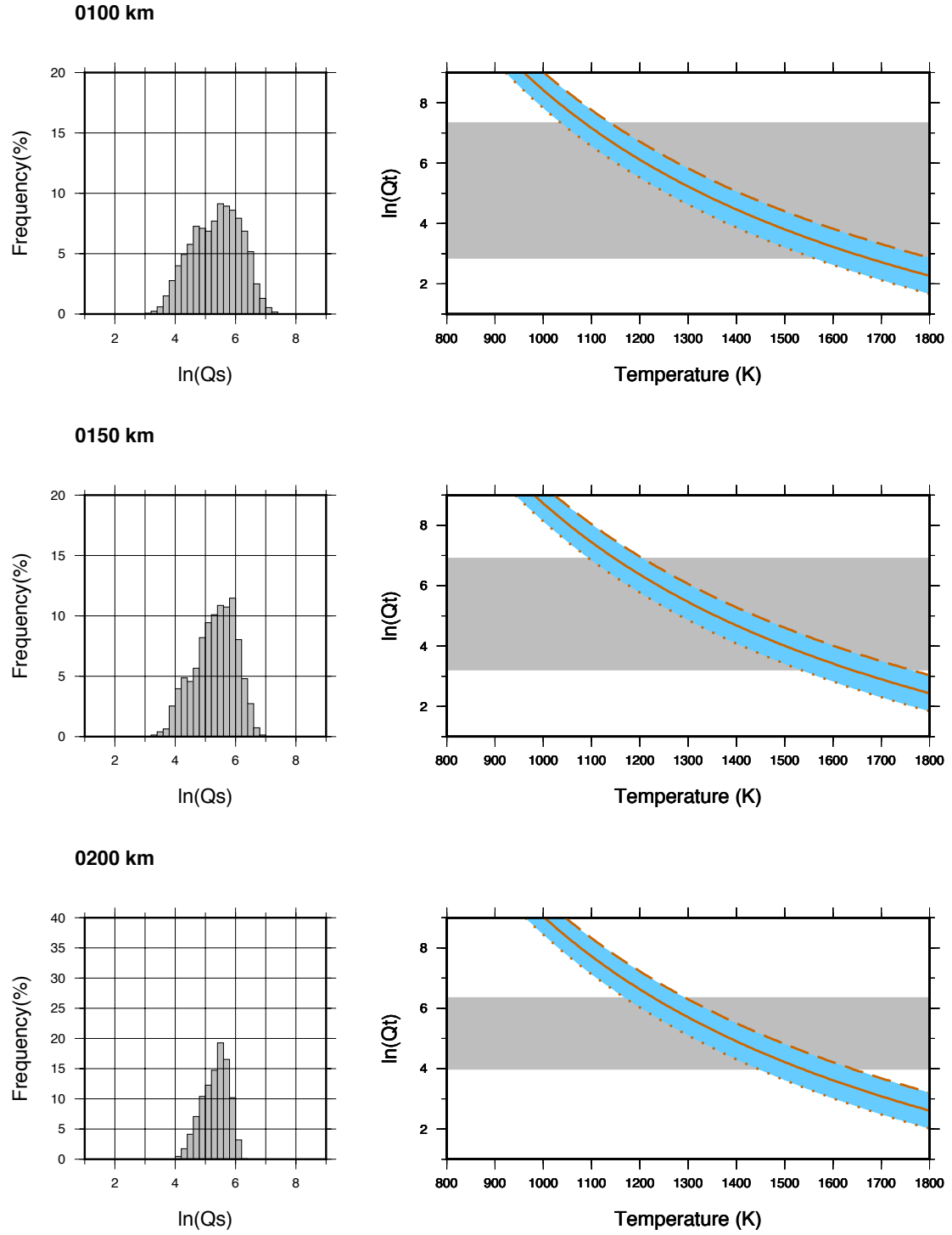


Fig. S7: Left column: Histograms of the distribution of  $\ln(Q_s)$  values extracted at 100 (top), 150 (middle) and 200 (bottom) km depth in QsADR17<sup>7</sup>. Right column: at the same depths, theoretical relation between  $\ln(Q_t)$  and temperature computed using Eq. A.1 for different grain sizes. The continuous lines in brown are the theoretical curves assuming a grain size of 10 mm. The light blue areas around this curve cover the influence of grain sizes from 1 mm (bottom dotted curve) to 100 mm (upper dashed curve). The shaded grey area shows the range of  $Q_s$  variations observed in QsADR17.

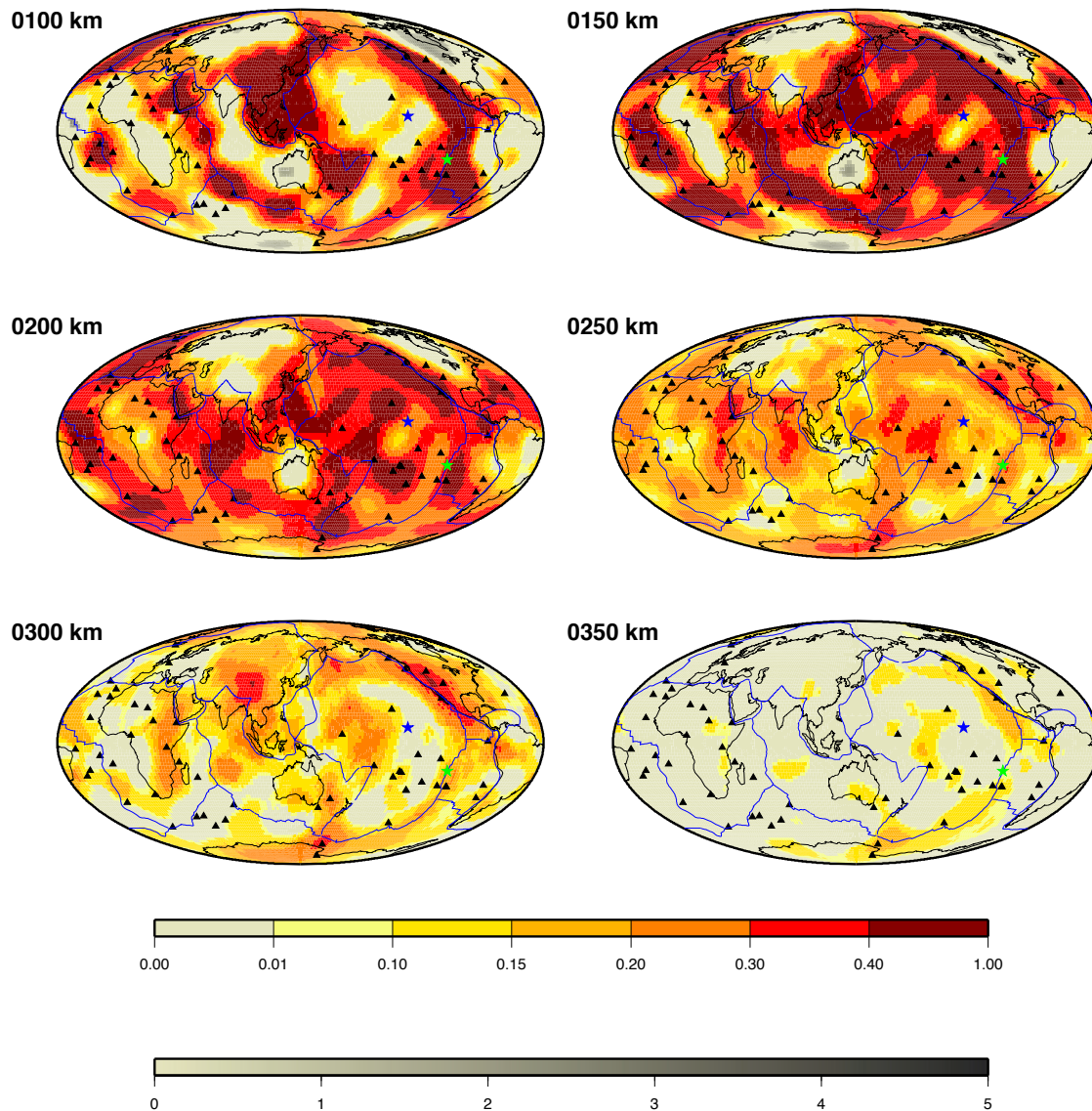


Fig. S8: same as Figure S2 but for a grain size of 100 mm.

### References :

1. Jackson, I., Fitz Gerald, J. D., Faul, U. H. & Tan, B. H. Grain-size-sensitive seismic wave attenuation in polycrystalline olivine. *J. Geophys. Res. Solid Earth* **107**, 2360 (2002).
2. Hammond, W. C. & Humphreys, E. D. Upper mantle seismic wave velocity: Effects of realistic partial melt geometries. *J. Geophys. Res. Solid Earth* **105**, 10975–10986 (2000).
3. Chantel, J. *et al.* Experimental evidence supports mantle partial melting in the asthenosphere. *Sci. Adv.* **2**, (2016).
4. Karato, S. Importance of anelasticity in the interpretation of seismic tomography. *Geophys. Res. Lett.* **20**, 1623–1626 (1993).

5. Dziewonski, A. M. & Anderson, D. L. Preliminary reference Earth model. *Phys. Earth Planet. Inter.* **25**, 297–356 (1981).
6. Takei, Y. Effects of Partial Melting on Seismic Velocity and Attenuation: A New Insight from Experiments. in *Annual Review of Earth and Planetary Sciences*, vol 45 (ed. Jeanloz, R and Freeman, K.) **45**, 447–470 (2017).
7. Adenis, A., Debayle, E. & Ricard, Y. Attenuation tomography of the upper mantle. *Geophys. Res. Lett.* **44**, (2017).